

<https://doi.org/10.1038/s43247-024-01408-5>

# Release and re-enrichment of invisible gold in arsenian pyrite promoted by coupled dissolution-reprecipitation reactions

Check for updates

Lin Yang<sup>1</sup>, Qingfei Wang<sup>1,2,3,4</sup> , Denis Fougerouse<sup>5</sup>, Haiyang Xian<sup>6</sup>, Huajian Li<sup>1</sup>, Ruixue Wang<sup>7</sup>, William D. A. Rickard<sup>5</sup>, David I. Groves<sup>1,8</sup> & Jun Deng<sup>1,3,4</sup>

The mechanisms responsible for invisible gold enrichment driven by coupled dissolution-reprecipitation reaction (CDR) are debated. Here we report the micro- to nano-scale textures of arsenian pyrite in a high-grade (>10 g/t) gold ore from the Chang'an deposit to trace the gold enrichment process. Our study records a CDR-driven evolution of mineral growth from an As-rich, Au-poor pyrite core, with numerous fine arsenopyrite inclusions, to an inclusion-free, As-Au-rich oscillatory pyrite rim. The reaction occurred at ~260 °C under 4.7 to 5.8 pH and -36.6 to -32.9 log<sub>f</sub>O<sub>2</sub> conditions. The elevated As but depleted S contents in the pyrite core indicate a combined elevation of S fugacity and solubility of Au. The coprecipitation of arsenopyrite inclusions in the core caused a depletion of S fugacity to -13.8 ~ -11.7, triggering Au enrichment in the rim. This non-unique process has the potential to explain the upgrade of invisible Au in arsenian sulfides, worldwide.

Gold in hydrothermal deposits occurs in a variety of forms including as native Au grains and invisible Au in arsenian sulfides<sup>1</sup>. Invisible Au consists of either disseminated atoms in the crystal lattice, nanoparticles, or decorates crystal defects in arsenian pyrite and arsenopyrite<sup>1-7</sup>. The extraordinary enrichment of visible Au, involving transportation, flocculation, and coarsening, has been well studied<sup>8-12</sup>, whereas that of invisible Au is debated due to the complex interaction of fluid physicochemical conditions and crystal growth processes. Incorporation of invisible Au into arsenian pyrite and arsenopyrite has commonly been suggested to be associated with growth kinetics of pyrite<sup>13,14</sup>, crystal defects induced by As incorporation<sup>4,15</sup>, and electrochemistry of crystal-fluid interfaces<sup>16-18</sup>. The liberation of invisible Au from arsenian sulfides has been attributed to a coupled dissolution-reprecipitation reaction (CDR)<sup>13,19-23</sup>. However, the mechanism of invisible Au enrichment driven

by the CDR of arsenian pyrite are poorly understood. These puzzles are partly due to the lack of micro- to nanoscale data illustrating the mechanisms operating at the boundaries between Au-poor and Au-rich pyrite and between inclusions and host pyrite.

Here we present the micro- to nano-scale texture of arsenian pyrite in a high-grade ore (>10 g/t) from the Chang'an epizonal orogenic gold deposit (>30 t Au; Fig. 1a)<sup>24</sup>. Mineralogical and geochemical evidence and thermodynamic modeling are presented to trace the growth processes of pyrite and the fluctuation of physicochemical conditions driven by CDR.

This study depicts a detailed evolution of mineral growth from As-rich, Au-poor pyrite core with numerous inclusions of arsenopyrite, to an inclusion-free, As-Au-rich pyrite rim. Fluctuation of physicochemical conditions controlled the release, remobilization, and reprecipitation of invisible Au into the pyrite rim.

<sup>1</sup>State Key Laboratory of Geological Processes and Mineral Resources, China University of Geosciences, Beijing 100083, China. <sup>2</sup>Jiangxi Provincial Key Laboratory of Genesis and Prospect for Strategic Minerals, East China University of Technology, Nanchang, Jiangxi 330013, China. <sup>3</sup>Geological Research Institute, Shandong Gold Group Co. Ltd., Jinan 250013, China. <sup>4</sup>Frontiers Science Center for Deep-time Digital Earth, China University of Geosciences (Beijing), Beijing 100083, China. <sup>5</sup>School of Earth and Planetary Sciences and John de Laeter Centre, Curtin University, Perth, WA, Australia. <sup>6</sup>CAS Key Laboratory of Mineralogy and Metallogeny/Guangdong Provincial Key Laboratory of Mineral Physics and Materials, Guangzhou Institute of Geochemistry, Chinese Academy of Sciences (CAS), Guangzhou 510640, China. <sup>7</sup>Commonwealth Scientific and Industrial Research Organization, Mineral Resources, Australian Resources Research Centre, Kensington, WA 6152, Australia. <sup>8</sup>Centre for Exploration Targeting, University of Western Australia, Crawley, WA 6009, Australia. e-mail: [wqf@cugb.edu.cn](mailto:wqf@cugb.edu.cn); [djun@cugb.edu.cn](mailto:djun@cugb.edu.cn)

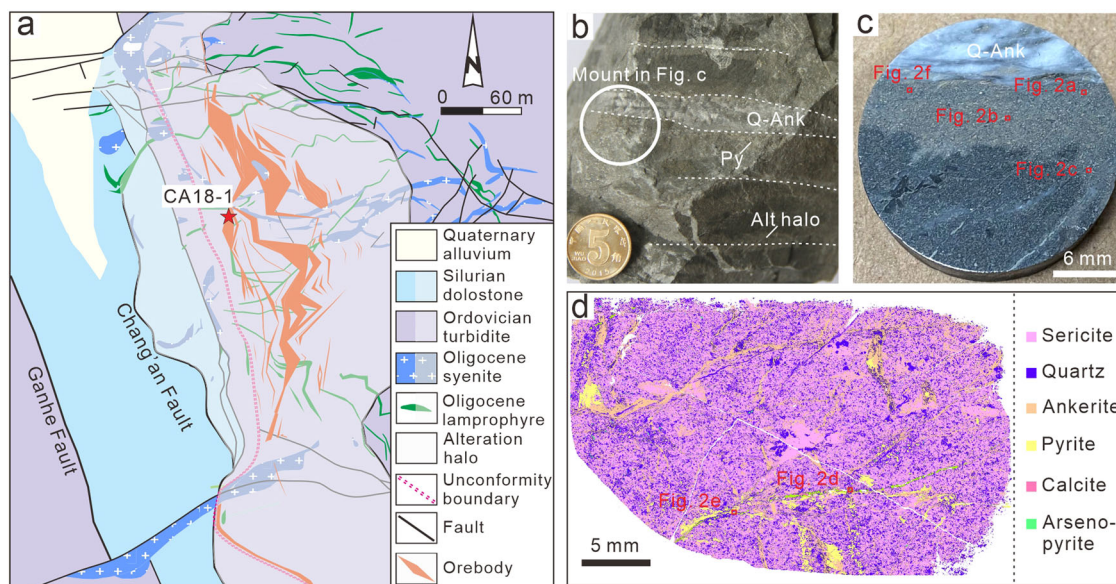


**Fig. 1 | Geological background, hand specimen, and alteration and mineralization types in the Chang'an gold deposit.** **a** Simplified geological map of the Chang'an gold deposit showing distribution of main rock units and faults, alteration zones and intrusions (modified from ref. 24). **b** Hand sample photograph of high-grade gold ore (CA18-1). The sample location has been shown in **(a)**. **c** A mount of

sample CA18-1 comprises quartz-ankerite veinlet, disseminated sulfides, and altered sandstone. The location is in **(b)**. **d** Mineral mapping of a thin section of sample CA18-1, showing alteration and mineralization patterns. The location is the same with the mount in **(b)**. Alt alteration, Ank ankerite, Py pyrite, Q quartz.

## Geological setting

The Chang'an gold deposit occurs in the southern segment of the Cenozoic Ailaoshan Orogen, the youngest orogenic gold belt globally<sup>25</sup>, located along the southeastern margin of the Tibetan Plateau<sup>26–28</sup> (Supplementary Fig. 1a). The main sedimentary units at Chang'an comprise an Ordovician turbidite package and Silurian dolostone (Fig. 1a; Supplementary Fig. 1b). The Ordovician turbidite package comprises a thick sequence of sandstone with minor thin layers of carbonaceous and calcareous sandstone, siltstone, mudstone, and conglomerate, among which the sandstone is the main host for the gold orebodies<sup>24,27</sup>. A series of ~35 Ma lamprophyre dikes and alkali-rich porphyry intrusions occur in the Chang'an gold deposit (Fig. 1a; Supplementary Fig. 1b)<sup>27</sup>. The gold orebodies which cross-cut the dikes are controlled by the NW–SE-trending Chang'an Fault (Fig. 1a; Supplementary Fig. 1b) and are discontinuous over 1.8 km along strike and 20–253 m down dip with an average grade of 4.54 g/t<sup>24</sup>. The crosscutting relationships the inferred stress field, and published paleomagnetic evidence, in combination, suggest that the Chang'an deposit most likely formed at ~23–21 Ma<sup>27,29,30</sup>. Geological characteristics at Chang'an include: (1) proximity to the major lithospheric-scale Ailaoshan shear zone, but ore zones hosted in second- or third-order Chang'an Fault; (2) gold-related alteration dominated by silicification, sericitization, sulfidation, and carbonation (Fig. 1b–d); and (3) lack of lateral metal zoning<sup>24,26,27</sup>. These features are compatible with those of orogenic gold deposits proposed by ref. 31, but differ from the extensional structures and ore textures of epithermal and Carlin-type gold deposits, as summarized by ref. 24.

## Results

### Pyrite texture and gold occurrence

The high-grade (>10 g/t) gold ores have a mineral assemblage of pyrite, arsenopyrite, galena, and sphalerite with minor native Au (Fig. 2a–f). The pyrite in the high-grade ores comprises commonly an As-rich core that contains fine-grained and numerous inclusions of arsenopyrite, sericite, galena, chalcopyrite, and native Au, and inclusion-free rim (Fig. 2a–f; Supplementary Fig. 2a–g). The pyrite rim is characterized by As oscillatory zoning (Fig. 2a–c). In localized domains, the oscillatory As zoning is dissected by As-poor pyrite

domains associated with arsenopyrite inclusions (0.1–5 μm; Fig. 2b). The pyrites from proximal to distal quartz-ankerite veinlet show a decline in arsenopyrite inclusions and thickness of pyrite rim (Fig. 2a–c). The ToF-SIMS analysis of pyrite grains with core and rim textures shows that the inclusion-rich pyrite core has high As contents relative to its rim and that Au is concentrated in the As-depleted, inclusion-free pyrite rim (Fig. 3a, b).

### Crystal relationship of fine-grained inclusions with host pyrite

The EBSD analysis reveals that the pyrite core and rim have similar crystallographic orientation (Fig. 3c–e). The analyzed pyrite has low-angle boundaries (<6° misorientation; Fig. 3e), which show no evidence of microfractures, indicating the coherent nature of the microstructure. The distribution of arsenopyrite inclusions is poorly correlated to the low-angle boundaries (white lines; Fig. 3e). Pole Figures of the {100}, {110}, and {111} crystal faces of arsenopyrite inclusions and its host pyrite show similar preferred crystallographic orientation (Fig. 3f, g).

### Geochemical composition of arsenopyrite

The EMPA shows that the fine-grained and anhedral arsenopyrite inclusions in the pyrite core have an atomic As concentration that range between 25.6% and 28.5% (median 27.7%;  $n = 40$ ), with corresponding variations in S content of 37.7–42.3% (median 38.7%) and Fe content of 31.1–34.3% (median 33.6%; Supplementary Table 1). In contrast, the As, S, and Fe concentrations in coarse-grained and euhedral arsenopyrite intergrown with pyrite range from 26.4% to 30.6% (median 28.9%;  $n = 11$ ), 36.1–41.1% (median 37.5%) and 33.2–33.8% (median 33.4%; Supplementary Table 1), respectively. There is an antithetic correlation between As and S ( $R^2 = 0.95$ ), indicating a coupled substitution within arsenopyrite, compatible with experimental studies<sup>32</sup>.

### Nano-scale texture and elemental mapping of pyrite

The high-angle annular dark field-scanning TEM (HAADF-STEM) analysis of the TEM foil identified a bright pyrite core with several bright arsenopyrite sub-micrometer particles and relative dark rim with few sub-micrometer particles (Fig. 4a; Supplementary Fig. 2a). The SAED patterns



**Fig. 2 | Representative pyrite texture in the Chang'an gold deposit.** a–f BSE images of pyrite comprising arsenopyrite-, galena- and void-rich core and inclusion-free rim. Pyrite quartz and native gold are wrapped by zoned pyrite in (d). The pyrites from proximal (a, f) to distal (b, c) quartz-ankerite veinlet show a decline in arsenopyrite inclusions and thickness of pyrite rim. The locations of (a–f) are shown in Fig. 1c, d. Alt alteration, Ank ankerite, Apy arsenopyrite, Au native gold, Ga galena, Py pyrite, Q quartz, Ser sericite.

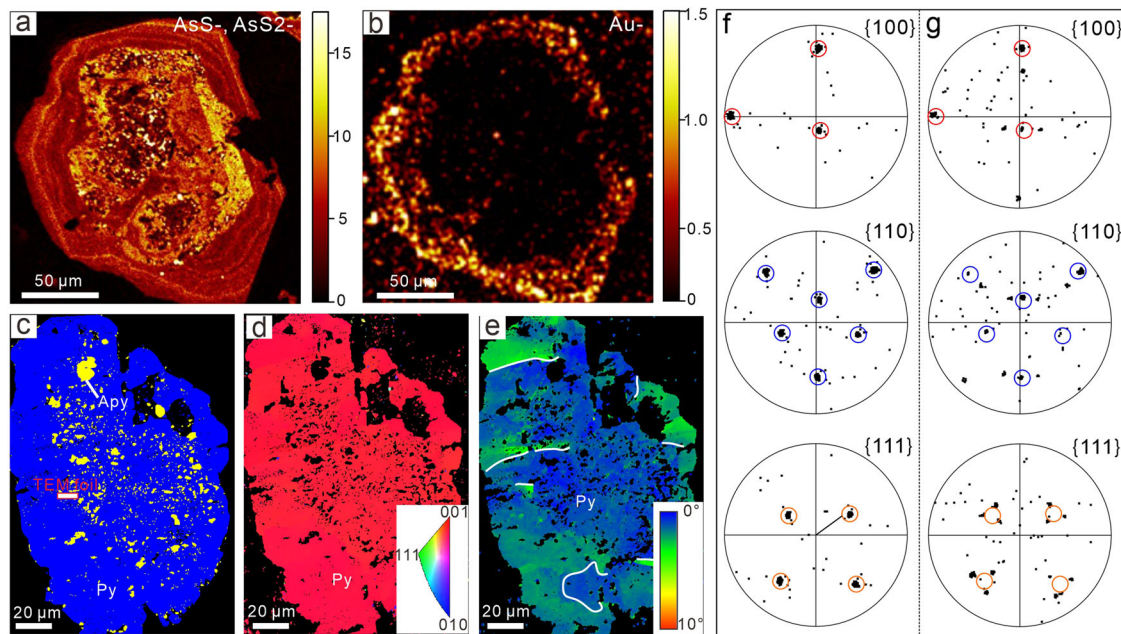
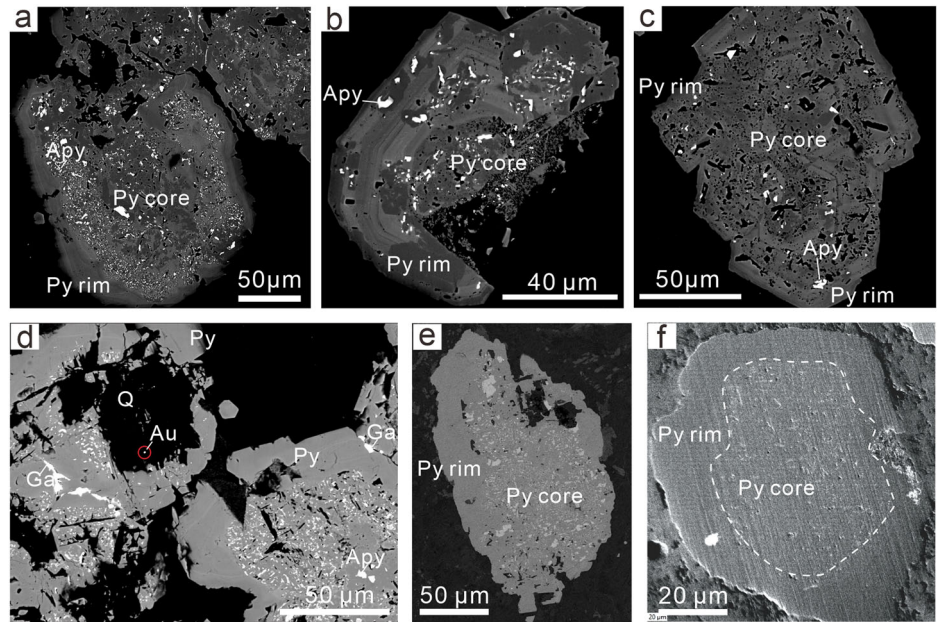


**Fig. 3 | Time-of-flight secondary ion mass spectrometry (ToF-SIMS) and EBSD maps of pyrites in high-grade Au ores, showing pyrite texture and gold distribution.** a Sum of AsS- and AsS2- and (b) Au- in pyrite grains with core and rim, showing gold is concentrated in the pyrite rim. The BSE image of the corresponding pyrite is shown in Fig. 2f. c Phase map showing distribution of arsenian pyrite and its arsenopyrite inclusions. The BSE image of the corresponding pyrite is shown in

Fig. 2e. d Inverse pole figure of pyrite along Z-direction displaying similar crystallographic orientation of the pyrite core and rim. e Grod angle figure showing the crystallographic misorientation of pyrite to a maximum of 6°. Low-angle boundaries (>1°) are plotted as white lines. f Polar diagram of arsenian pyrite. g Polar diagram of arsenopyrite inclusions within the host pyrite, showing their preferred orientation.

and high-resolution TEM (HRTEM) images of the pyrite core and rim indicate that they have coherent crystal lattice (Fig. 4b, c), but that the pyrite core is characterized by abundant stacking faults relative to the pyrite rim, as shown by the HAADF-STEM image (Fig. 4a). The arsenopyrite particles with 50 nm to 1.5 μm diameter are located along the microfractures and/or voids of the pyrite core (Fig. 4a, c; Supplementary Fig. 2d–f) and host coherent crystal lattice with the pyrite core (Fig. 4d). The HAADF-STEM image and corresponding EDS maps show that the pyrite core has heterogeneous Fe and As contents but that the pyrite surrounding a sericite inclusion has a high As content, but low Fe and S contents (Fig. 4e, f).

## Discussion

### Genesis of pyrite texture

The fine-grained and numerous arsenopyrite, galena, chalcopyrite, and native Au inclusions in arsenian pyrite from the Chang'an gold deposit can be attributed to post-crystallization exsolution of solid solution from metastable arsenian pyrite<sup>2,33</sup> or fluid-mediated CDR<sup>20,21</sup>. If the former is correct, stacking faults in the high-As pyrite core would represent the lowest energy site for the nucleation of the arsenopyrite inclusions<sup>34</sup>. However, no systematic relationship between the high density of stacking faults in the high-As core and the location of the inclusions is recorded at Chang'an

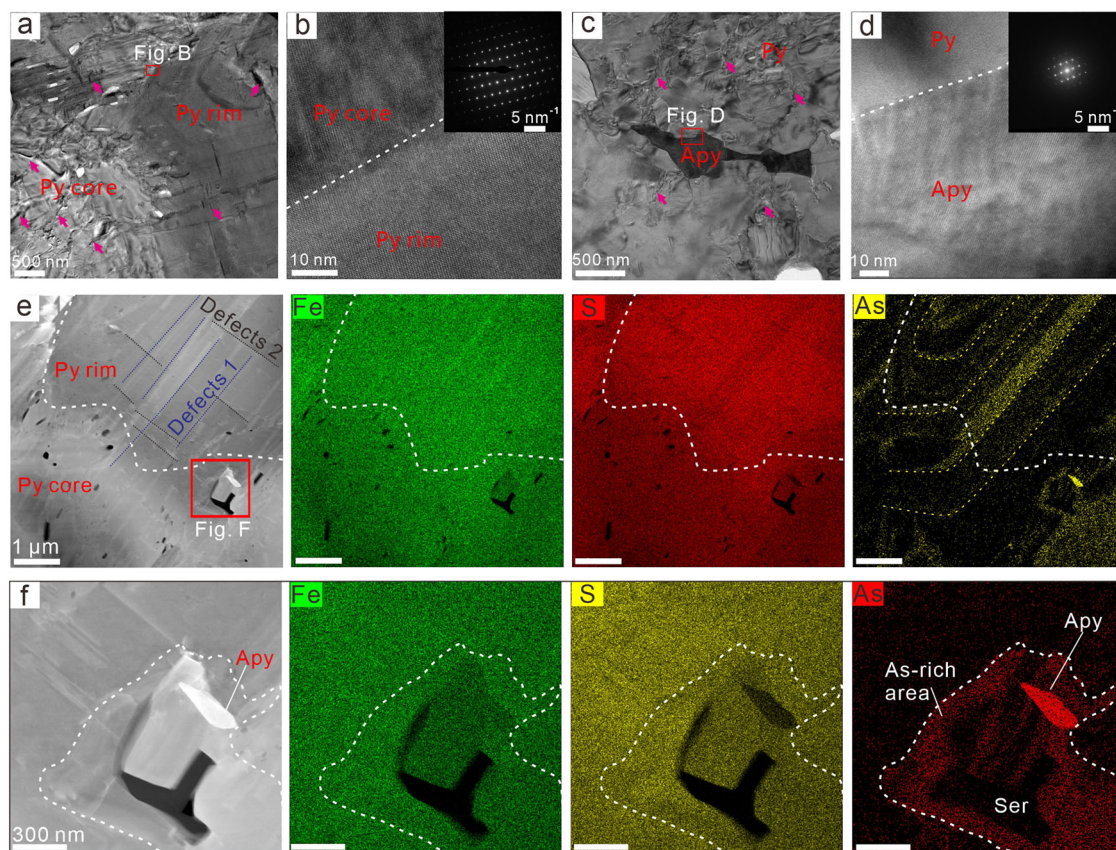


**Fig. 4 | TEM and HRTEM images and HAADF-STEM image and corresponding EDS maps. a** Bright field (BF) TEM image showing stacking faults (pink arrows) in pyrite core and rim. **b** HRTEM image showing that the pyrite core and rim share the same crystal orientation. The inset shows the SAED pattern from the zone including both core and rim. **c** BF TEM image showing stacking faults in pyrite core and arsenopyrite grown along a microfracture in pyrite. **d** HRTEM image showing that pyrite core and arsenopyrite share the same crystal orientation. The inset shows the

corresponding fast Fourier transformation (FFT) pattern. **e** Pyrite core with micro-porosity, arsenopyrite, and sericite inclusions, and rim with As-oscillatory zoning. Defects 2 (blue dashed lines) crosscut defects 1 (black dashed lines). **f** HAADF-STEM image and the corresponding EDS maps of pyrite core and its arsenopyrite and sericite inclusions, showing that pyrite surrounding sericite has a high As content.

(Fig. 4a, c). Considering the sharp boundary between As-rich and As-poor pyrite, and truncation of the oscillatory zoning, a crystallographic relationship between the pyrite and arsenopyrite inclusions can be predicted from the pseudomorphic CDR model<sup>20</sup>. The EBSD and TEM data reveal a similar preferred crystallographic orientation and coherent grain boundaries between the arsenopyrite inclusions and the pyrite core (Figs. 3f–g, 4d; Supplementary Fig. 2b, c). This relationship supports the replacement of the As-bearing pyrite core by As-poor pyrite and arsenopyrite via a CDR reaction at Chang'an, as reported in other gold deposits worldwide<sup>13,14,21</sup>.

The heterogeneous Fe distribution in the pyrite core (Fig. 4e, f) can be explained by an interaction between the ore fluids and pyrite. The deposition of pyrites that comprise cores and rims with contrasting trace element compositions in gold deposits has mostly been attributed to the involvement of multi-pulses of fluids<sup>35</sup>. At Chang'an, two different crystal defects 1 and 2 have been identified in the investigated pyrite with defects 1 that crosscut defects 2 (Fig. 4e). The elongated defects 1 are aligned perpendicular to crystal faces which implies that their formation is related to crystal growth, which is normal for growth-related stacking faults<sup>36</sup>. However, the high As zones are parallel to defects 1 and extend almost at right-angles across the boundary between the inclusion-rich core and inclusion-free rim of pyrite (Fig. 4e), indicating continuous precipitation of the As zone from the core to the rim. This phenomenon, together with lack of evidence for overlapping alteration and mineralization related to multi-pulse fluids in the gold ores (Fig. 1c), suggests that a single-pulse fluid was responsible for the CDR and pyrite textures at Chang'an.

### Microenvironment for the CDR of arsenian pyrite

The As content of arsenopyrite and phase relationships of arsenian pyrite and arsenopyrite indicate that the formation temperature of euhedral arsenopyrite was mostly from 299 °C to 290 °C (median 294 °C) with two anomalous values of 350 °C and 325 °C, whereas temperatures of fine-grained and anhedral arsenopyrite inclusions within pyrite core are 272 °C to 256 °C (median 264 °C; Fig. 5a). The temperature of the CDR of arsenian pyrite can thus be better constrained at ~260 °C. The phase diagram in Fig. 5a shows that the S fugacity ( $f_{S_2}$ ) of these fine-grained arsenopyrite inclusions is about -13.8 to -11.7, which is lower than those of euhedral arsenopyrite with values of -11.9 to -10.2 (except for two anomalous values; Fig. 5a).

Considering the 1.3–4.6 km emplacement depth of alkali-rich porphyries located <1.5 km from the Chang'an deposit based on the hornblende thermobarometer<sup>37</sup>, the CDR temperature of ~260 °C, and the epizonal mineralization types<sup>24</sup>, the modeled pressure was set at ~1 kbar. Based on the low sulfide content, sericite (muscovite)–ankerite alteration, and <6 wt% NaCl equiv salinities for typical orogenic gold deposits, we set the following of  $m_{SS} = 0.01$ ,  $m_{K^+} = 0.005$ ,  $m_{Fe^{2+}} = 0.0005$ ,  $m_{Ca(HCO_3)} = 0.00005$ , and  $m_{Cl^-} = 1$ . The pH and  $f_{O_2}$  conditions of alteration and ore mineral precipitation are constrained by phase stability relationships using SUPCRT92<sup>38</sup> and values of pH are calculated from mineral equilibria in the system K-Na-Ca-Fe-Cu-Al-O-H-S. The ankerite, sericite, and quartz alteration assemblages indicate a wide pH range, 4.7–5.8, of the ore fluids during mineral precipitation (Fig. 5b). Formation of mineral assemblages of



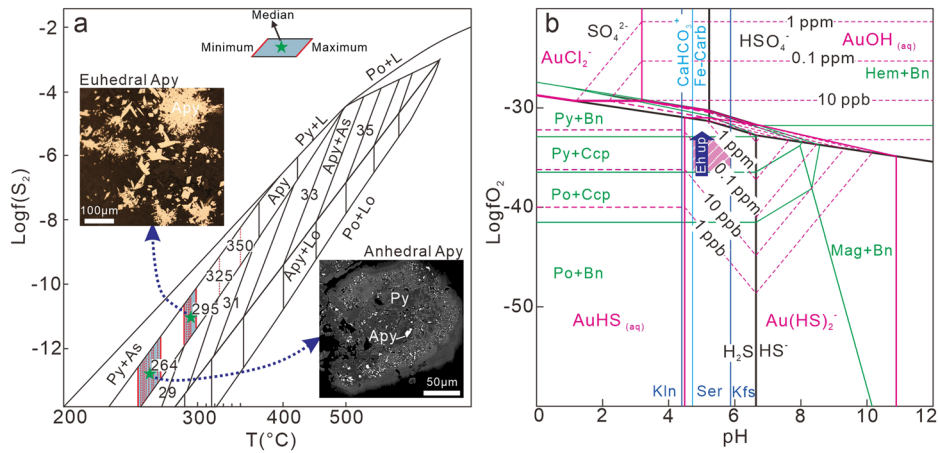
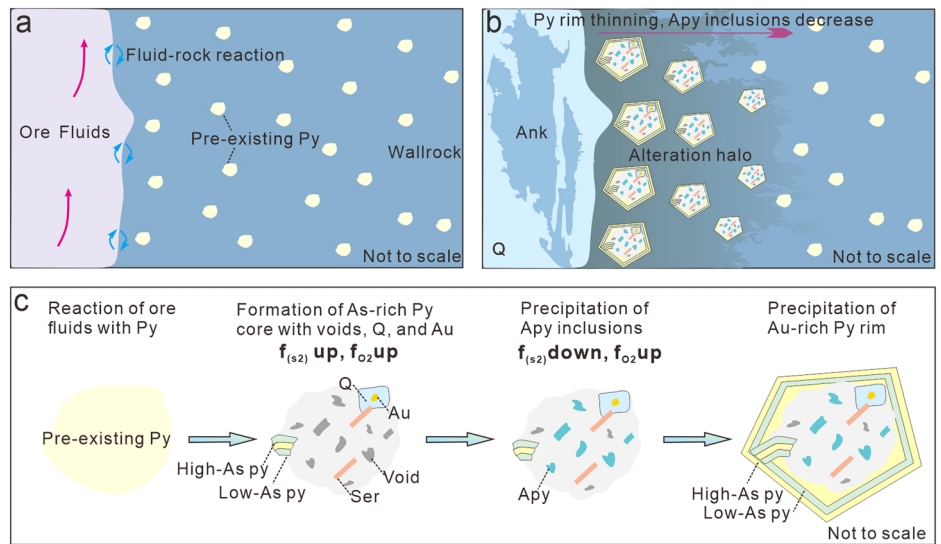


**Fig. 5 | Phase diagram showing the physicochemical conditions of the formation of pyrite and arsenopyrite.** **a** Phase diagram of the Fe-As-S system in temperature (T)- $f_{S_2}$  space, modified after ref. 19. The red solid lines indicate the stability field of the euhedral arsenopyrite (shown in top lefthand corner) and pyrite assemblage under a temperature range of 299–290 °C (median 294 °C with two anomalous values of 350 °C and 325 °C). The stability field of fine-grained and anhedral arsenopyrite (shown in bottom righthand corner) inclusions and pyrite assemblage under a temperature range of 272–256 °C (median 264 °C). The red dash lines represent data from each of the analyzed arsenopyrites. **b**  $\text{Log}f_{O_2}$  versus pH diagrams showing stability relationships in the Fe-Cu-O-S system at 260 °C and 1 kbar.

The phase diagram was constructed assuming  $m_{SS} = 0.01$ ,  $m_{K^+} = 0.005$ ,  $m_{Fe^{2+}} = 0.0005$ ,  $m_{Ca(HCO_3)^+} = 0.00005$ , and  $m_{Cl^-} = 1$ . The thick black lines represent the normal boundaries of the principal aqueous sulfur species and the blue lines the stability boundaries for pyrite (Py), pyrrhotite (Po), hematite (Hem), magnetite (Mag), chalcopyrite (Ccp), and bornite (Bn). The stability boundaries for K-feldspar (Kfs)–sericite, sericite-kaolinite (Kln), and  $\text{CaHCO}_3^+$ -Fe-carbonate are also shown, according to refs. 46,47. The pink solid lines indicate the boundary of the predominant Au (with 1 ppb–10 ppm Au in the solution, as marked by the pink dash lines). Apy arsenopyrite, L liquid, Lo lollingite, Po pyrrhotite, Py pyrite.

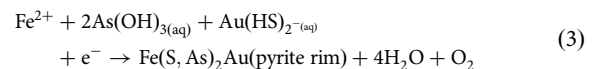
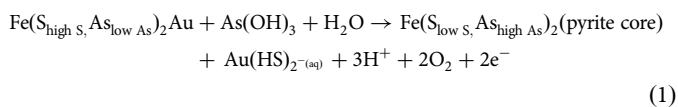
**Fig. 6 | A cartoon showing the ore-zone scale fluid-rock interaction and the micro- to nano-scale process of dissolution-precipitation reactions responsible for Au enrichment in the Chang’an gold deposit.** **a** Ore fluid infiltration and fluid-rock reaction. **b** Formation of quartz-ankerite veinlets and alteration haloes as well as the distribution of pyrite. **c** Detailed process of pyrite growth and Au enrichment associated with dissolution-precipitation reaction. Note that replacement of pre-existing arsenian pyrite by porous pyrite, with sericite inclusions and overgrown quartz and native gold, is interpreted to have triggered elevated O and S fugacities promoting Au solution at the interface between fluid and pyrite. Precipitation of abundant fine-grained arsenopyrite aggregates in the voids within the pyrite core is considered to have resulted in a decrease in S fugacity and thus triggered Au deposition in pyrite rim. Ank ankerite, Au native gold, Py pyrite, Q quartz, Ser sericite.



pyrite-chalcopyrite-galena required  $\text{log}f_{O_2}$  values between  $-36.6$  and  $-32.9$  (Fig. 5b).

**Invisible Au enrichment and implications**

The ore fluids infiltrated and reacted with the sandstone and its hosted pre-existing pyrite to form quartz-ankerite veinlets and alteration haloes with invisible Au-bearing arsenian pyrite at Chang’an (Fig. 6a, b). As noted above, the complex pyrite textures can be explained as pseudomorphic replacement of arsenian pyrite by fluid-mediated CDR. Considering the pyrite texture and the mineral assemblage, the relevant reactions are:



The syn-sedimentary and pre-existing different generations of pyrite generally have low As contents with mean values ranging from 620.8 ppm to 8931 ppm at Chang’an<sup>24</sup>. The cores of hydrothermal pyrite have elevated As contents with a mean value of 11,325 ppm<sup>24</sup>, and depleted S and Fe contents relative to pre-existing pyrite that was dissolved during the fluid-mediated CDR process (Fig. 4e, f). It resulted in an increase in S in the ore fluids, especially at fluid-crystal interfaces, and thus increased the solubility of gold as an  $\text{Au}(\text{HS})_2^-$  complex<sup>19,39</sup>. The reaction may also cause an increase in O

fugacity, as illustrated by a decreasing trend in  $\delta^{34}\text{S}$  values from pyrite core to pyrite rim<sup>24</sup>. The increase in O fugacity would have promoted residence of Au in the ore fluids as shown in Fig. 5b. The abundant crystal defects (e.g., stacking faults and dislocations) in the pyrite core can be attributed to either or both of the heterogeneous As incorporation into lattice crystal growth in pyrite<sup>6</sup> and lattice deformation driven by stress and fluid pressure, or both<sup>36</sup>. The sericite and quartz were deposited along stacking faults in the pyrite core (Fig. 4a), indicative of a cogenetic relationship between them. The minor native Au overgrown with quartz wrapped in the pyrite core can be attributed to the deposition of Au and quartz from ore fluids due to local supersaturation in Au and Si<sup>13</sup>.

HAADF-STEM images show that arsenopyrite inclusions grew along microfractures of the pyrite core (Fig. 4c), suggesting that the fine-grained arsenopyrite inclusions precipitated later than its formation. The equation for reaction 2 demonstrates that the deposition of arsenopyrite inclusions in pores within the pyrite core would have consumed the Fe, As, and S and thus result in a decrease in S fugacity. This inference is supported by the decreased S fugacity of  $-13.8$  to  $-11.7$  for the precipitation of arsenopyrite inclusions formed by the CDR, which is lower than that of the euhedral arsenopyrite and intergrown pyrite that were precipitated directly from the ore fluids ( $-11.9$  to  $-10.2$ ; Fig. 5a). The interpreted decrease in S fugacity would have triggered the deposition of invisible Au in the oscillatory As-zoned pyrite rims (Fig. 6c). Gold in the pyrite rims is dominantly in solid-solution, indicating that the ore fluid was still undersaturated with Au after the precipitation of the arsenopyrite inclusions. The incorporation of Au in pyrite rims with Au-As zoning (reaction 3) can be attributed to processes operating at the mineral surfaces and the growth rate of pyrite, as reported in other cases worldwide<sup>4,14,40,41</sup>.

This study records a detailed process of mineral growth, fluctuation of physicochemical conditions, and final Au incorporation into pyrite rims associated with the CDR at the micro- to nano-scale. At the ore scale, there is a decline in the concentration of arsenopyrite inclusions, thickness of pyrite rims, and thus gold concentration, from proximal to distal quartz-ankerite veinlets (Fig. 2a–c, f), which can be attributed to a decline in ore fluid: rock ratios. High fluid-rock ratios are likely a pivotal factor for upgrade of invisible Au during CDR reactions, as supported by the thermodynamic modeling by ref. 42. The pyrite textures at Chang'an are similar to those of Sunrise Dam<sup>21</sup> and Kanowna Belle gold deposits<sup>43</sup> in Western Australia and Konkera gold deposit in West Africa<sup>44</sup>, suggesting that the process of Au release, remobilization, and re-enrichment noted above is not unique.

## Methods

### Geological sampling

The high-grade (>10 g/t) gold ores (CA18-1) are hosted in the sandstone, which is cut by a series of sub-parallel centimeter-scale quartz-sulfide veinlets associated with sericite alteration haloes (Fig. 1c, d). The sample CA18-1 was collected from the 1532 m level and the location has been marked in Fig. 1a and Supplementary Fig. 1b.

### Scanning electron microscope (SEM) and electron back-scattered diffraction (EBSD) analyses

Thin sections and polished mounts of studied samples were examined under an optical microscope and SEM to determine mineral textures and paragenesis. Analyses of SEM were carried out in the Key Laboratory of Deep-Earth Dynamics, Institute of Geology, Chinese Academy of Geological Sciences, using a FEI Nova NanoSEM 450. The backscattered electron (BSE) imaging was taken under an operating voltage of 15–20 KV and the working distance of 13.5 mm. Crystallographic orientation analysis was carried out using an EBSD detector installed at a field emission SEM system at the SEM-EBSD Laboratory, School of Earth Sciences, China University of Geosciences (Wuhan). Working conditions were as follows: 20 kV accelerating voltage, 0.1–0.3 spot size, working distance of 20 mm, 70° sample tilt angle, and low-vacuum mode of 20 Pa. Diffraction patterns were collected and indexed with an automatic mapping mode using the Aztec 4.0 software from the Oxford Instruments.

### TESCAN integrated mineral analyzer (TIMA) and electron probe microanalysis (EMPA)

Alteration types and crosscutting relationships were analyzed using TIMA at the Guangzhou Tuoyan Analytical Technology Co., Ltd. An acceleration voltage of 25 kV and a beam current of 8.24 nA were used with working distance of 15 mm. Pixel spacing and dot spacing were 3  $\mu\text{m}$  and 9  $\mu\text{m}$ , respectively. The samples were scanned using TIMA liberation analysis module. Major element components of arsenopyrite were analyzed at Craton Science and Technology Co., LTD, Beijing, using a JXA-8230 electron microprobe. Working conditions include a voltage of 15 kV, beam current of  $2 \times 10^{-8}$  A, spot size of 1  $\mu\text{m}$ , and detection limit of 0.01%. Analytical results were reduced using the ZAF (Z, atomic number; A, absorption; F, fluorescence) correction routines.

### Time-of-flight secondary ion mass spectrometry (ToF-SIMS) microanalysis

The ToF-SIMS of arsenian pyrite was performed using the IONTOF M6 instrument in the John de Laeter Centre at Curtin University, Australia. The instrument was operated in Fast Imaging mode with a 60 kV  $\text{Bi}_3^{++}$  primary ion source at a pulsed current of 0.2 pA. Negative ions were collected using Delayed Extraction mode for the mass analyzer at a cycle time of 50  $\mu\text{s}$ . SIMS maps were collected over a  $350 \times 350 \mu\text{m}$  field of view with  $1024 \times 1024$  pixels in each frame (342 nm pixel size). To remove surface contamination and increase the ionization rate, the field of view was pre-sputtered with a  $\text{Cs}^+$  ion source (2 kV, 70 nA) over a  $500 \times 500 \mu\text{m}$  area for 60 s. Analysis time was 50 min where 60 frames were collected over the analyzed region.

### Transmission electron microscopy (TEM) observation and analyses

Two regions of interest cutting the boundaries of Au-poor pyrite core and Au-rich pyrite rim were extracted using Focused ion beam (FIB) micro-sampling on a Zeiss Auriga Compact instrument at the Institute of Geology and Geophysics, Beijing, China. The steps that select the sites of interest (Supplementary Fig. 3a, e), cut and remove the foil from its excavation site (Supplementary Fig. 3b, c, f, g), and mount the foil on the Cu-grid (Supplementary Fig. 3d, h) in the preparation of site-specific TEM foils are shown in Supplementary Fig. 3. The TEM analyses for nano-scale mineral texture and elemental mapping by the Energy Dispersive Spectrometer (EDS) were performed at Electron Microscopy Center of GIGCAS, using a ThermoFisher FEI Talos F200S microscope. A Ceta 16 M camera and TEM image analysis software (Thermo Fisher Scientific) were used to capture and analyze the TEM images, respectively. A 10  $\mu\text{m}$  selective area aperture under the microscope mode in the TEM system was used to record the selected area electron diffraction (SAED) patterns. The scanning transmission electron microscopy (STEM) system was used to record the EDS spectra and elemental maps and the EDS quantifications were performed at a beam current of 1 nA using the Thermo Fisher Scientific software either with or without standards. The uncertainty of Fe and S were <0.5%.

### Data availability

Source data that support the findings of this study are available in figshare with the identifier <https://doi.org/10.6084/m9.figshare.25471537.v1><sup>45</sup>.

Received: 5 August 2023; Accepted: 19 April 2024;

Published online: 08 May 2024

## References

1. Large, R. R. & Maslennikov, V. V. Invisible gold paragenesis and geochemistry in pyrite from orogenic and sediment-hosted gold deposits. *Minerals* **10**, 339 (2020).
2. Palenik, C. S. et al. Invisible" gold revealed: Direct imaging of gold nanoparticles in a Carlin-type deposit. *Am. Mineral.* **89**, 1359–1366 (2004).

3. Cline, J. S., Hofstra, A. H., Muntean, J. L., Tosdal, R. M. & Hickey, K. A. Carlin-type gold deposits in Nevada critical geologic characteristics and viable models. *Econ. Geol.* 100th Anniv. 451–484 (2005).
4. Reich, M. et al. Solubility of gold in arsenian pyrite. *Geochim. Cosmochim. Acta* **69**, 2781–2796 (2005).
5. Large, R. R. et al. Gold and trace element zonation in pyrite using a laser imaging technique: implications for the timing of gold in orogenic and carlin-style sediment-hosted deposits. *Econ. Geol.* **104**, 635–668 (2009).
6. Fougereuse, D. et al. A new kind of invisible gold in pyrite hosted in deformation-related dislocations. *Geology* **49**, 1225–1229 (2021).
7. Liang, Q.-L. et al. Evolution of invisible Au in arsenian pyrite in Carlin-type Au deposits. *Econ. Geol.* **116**, 515–526 (2021).
8. Hastie, E. C. G., Kontak, D. J. & Lafrance, B. Gold Remobilization: insights from gold deposits in the archaean swazye greenstone belt, abitibi subprovince. *Canada. Econ. Geol.* **115**, 241–277 (2020).
9. Hastie, E. C. G., Schindler, M., Kontak, D. J. & Lafrance, B. Transport and coarsening of gold nanoparticles in an orogenic deposit by dissolution–reprecipitation and Ostwald ripening. *Commun. Earth. Environ.* **2**, 57 (2021).
10. McLeish, D. F., Williams-Jones, A. E., Vasyukova, O. V., Clark, J. R. & Board, W. S. Colloidal transport and flocculation are the cause of the hyperenrichment of gold in nature. *Proc. Natl. Acad. Sci. USA* **118**, e2100689118 (2021).
11. Petrella, L. et al. Nanoparticle suspensions from carbon-rich fluid make high-grade gold deposits. *Nat. Commun.* **13**, 3795 (2022).
12. Xian, H. et al. Hyperenrichment of gold in pyrite induced by solid-state transportation. *Commun. Earth. Environ.* **3**, 308 (2022).
13. Fougereuse, D. et al. Gold remobilisation and formation of high grade ore shoots driven by dissolution-reprecipitation replacement and Ni substitution into auriferous arsenopyrite. *Geochim. Cosmochim. Acta* **178**, 143–159 (2016).
14. Wu, Y.-F. et al. Metal remobilization and ore-fluid perturbation during episodic replacement of auriferous pyrite from an epizonal orogenic gold deposit. *Geochim. Cosmochim. Acta* **245**, 98–117 (2019).
15. Gopon, P. et al. A nanoscale investigation of carlin-type gold deposits: an atom-scale elemental and isotopic perspective. *Econ. Geol.* **114**, 1123–1133 (2019).
16. Widler, A. M. & Seward, T. M. The adsorption of gold(I) hydrosulphide complexes by iron sulphide surfaces. *Geochim. Cosmochim. Acta* **66**, 383–402 (2002).
17. Mikhlin, Y. L., Romanchenko, A. S. & Asanov, I. P. Oxidation of arsenopyrite and deposition of gold on the oxidized surfaces: A scanning probe microscopy, tunneling spectroscopy and XPS study. *Geochim. Cosmochim. Acta* **70**, 4874–4888 (2006).
18. Becker, U., Reich, M. & Biswas, S. Nanoparticle-host interactions in natural systems. in *Nanoscope Approaches in Earth and Planetary Sciences* (eds Ferraris, G., Brenker, F. E. & Jordan, G.) 325–376 (Mineralogical Society of Great Britain and Ireland, 2010).
19. Morey, A. A., Tomkins, A. G., Bierlein, F. P., Weinberg, R. F. & Davidson, G. J. Bimodal distribution of gold in pyrite and arsenopyrite: examples from the Archaean Boorara and Bardoc shear systems, Yilgarn Craton, Western Australia. *Econ. Geol.* **103**, 599–614 (2008).
20. Putnis, A. Mineral replacement reactions. *Rev. Mineral. Geochem.* **70**, 87–124 (2009).
21. Sung, Y.-H. et al. Invisible gold in arsenian pyrite and arsenopyrite from a multistage Archaean gold deposit: Sunrise Dam, Eastern Goldfields Province, Western Australia. *Miner. Deposita* **44**, 765–791 (2009).
22. Atree-Williams, A., Pring, A., Ngothai, Y. & Brugger, J. Textural and compositional complexities resulting from coupled dissolution–reprecipitation reactions in geomaterials. *Earth-Sci. Rev.* **150**, 628–651 (2015).
23. Konrad-Schmolke, M. et al. Mineral dissolution and reprecipitation mediated by an amorphous phase. *Nat. Commun.* **9**, 1637 (2018).
24. Yang, L. et al. Fluid source and metal precipitation mechanism of sediment-hosted Chang’an orogenic gold deposit, SW China: Constraints from sulfide texture, trace element, S, Pb, and He-Ar isotopes and calcite C-O isotopes. *Am. Mineral.* **106**, 410–429 (2021).
25. Goldfarb, R. J., Groves, D. I. & Gardoll, S. Orogenic gold and geologic time: a global synthesis. *Ore. Geol. Rev.* **18**, 1–75 (2001).
26. Wang, Q. et al. Evolution of the Miocene Ailaoshan orogenic gold deposits, southeastern Tibet, during a complex tectonic history of lithosphere–crust interaction. *Miner. Deposita* **55**, 1085–1104 (2020).
27. Yang, L. et al. Multiple orogenic gold mineralization events in a collisional orogen: insights from an extruded terrane along the southeastern margin of the Tibetan Plateau. *J. Structl. Geol.* **147**, 104333 (2021).
28. Deng, J. et al. Tibetan ore deposits: a conjunction of accretionary orogeny and continental collision. *Earth-Sci. Rev.* **235**, 104245 (2022).
29. Wang, Q. F. et al. Towards a universal model for orogenic gold systems: a perspective based on Chinese examples with geodynamic, temporal, and deposit-scale structural and geochemical diversity. *Earth-Sci. Rev.* **224**, 103861 (2022).
30. Gao, L., Wang, Q., Deng, J., Zhang, S. & Yang, Z. Relationship Between Orogenic Gold Mineralization and Crustal Shearing Along Ailaoshan-Red River Belt, Southeastern Tibetan Plateau: New Constraint From Paleomagnetism. *Geochim. Geophys. Geosyst.* **19**, 2225–2242 (2018).
31. Groves, D. I., Goldfarb, R. J., Gebre-Mariam, M., Hagemann, S. G. & Robert, F. Orogenic gold deposits: a proposed classification in the context of their crustal distribution and relationship to other gold deposit types. *Ore. Geol. Rev.* **13**, 7–27 (1998).
32. Sharp, Z. D., Essene, E. J. & Kelly, W. C. A re-examination of the arsenopyrite geothermometer; pressure considerations and applications to natural assemblages. *Can. Mineral.* **23**, 517–534 (1985).
33. Stepanov, A. S. et al. Phase relations of arsenian pyrite and arsenopyrite. *Ore. Geol. Rev.* **136**, 104285 (2021).
34. Dubosq, R., Rogowitz, A., Schweinar, K., Gault, B. & Schneider, D. A. A 2D and 3D nanostructural study of naturally deformed pyrite: assessing the links between trace element mobility and defect structures. *Contrib. Mineral. Petrol.* **174**, 72 (2019).
35. Peterson, E. C. & Mavrogenes, J. A. Linking high-grade gold mineralization to earthquake-induced fault-valve processes in the Porgera gold deposit, Papua New Guinea. *Geology* **42**, 383–386 (2014).
36. Börner, F. et al. Between defects and inclusions: the fate of tellurium in pyrite. *Chem. Geol.* **635**, 121633 (2023).
37. Deng, J., Xin, W., Mao, G. & Li, L. Contribution of magmatic rocks to skarn Cu-Mo mineralization: a case study of Chang’an chong Cu-Mo deposit in Jinping, Yunnan Province. *Chin. J. Geol.* **58**, 598–616 (2023).
38. Johnson, J. W., Oelkers, E. H. & Helgeson, H. C. SUPCRT92: a software package for calculating the standard molal thermodynamic properties of minerals, gases, aqueous species, and reactions from 1 to 5000 bar and 0 to 1000°C. *Comput. Geosci.* **18**, 899–947 (1992).
39. Liu, W. et al. Gold transport in hydrothermal fluids: competition among the Cl<sup>-</sup>, Br<sup>-</sup>, HS<sup>-</sup> and NH<sub>3</sub>(aq) ligands. *Chem. Geol.* **376**, 11–19 (2014).
40. Kusebauch, C., Gleeson, S. A. & Oelze, M. Coupled partitioning of Au and As into pyrite controls formation of giant Au deposits. *Sci. Adv.* **5**, eaav5891 (2019).
41. Ishida, M. et al. Auriferous pyrite formed by episodic fluid inputs in the Akeshi and Kasuga high-sulfidation deposits, Southern Kyushu, Japan. *Miner. Deposita* **57**, 129–145 (2022).
42. Xing, Y., Brugger, J., Tomkins, A. & Shvarov, Y. Arsenic evolution as a tool for understanding formation of pyritic gold ores. *Geology* **47**, e335–e338 (2019).
43. Sugiono, D. et al. Integration of multiple sulfur isotopes with structural analysis unveils the evolution of ore fluids and source of sulfur at the

- Kanowna Belle Archean orogenic gold deposit, Yilgarn Craton, Western Australia. *Miner. Deposita* **56**, 1471–1490 (2021).
44. Goemann, K., Stepanov, A. S., Meffre, S. & Large, R. R. Gold and arsenopyrite exsolution and limits of arsenic solubility in pyrite investigated by SEM, EPMA, and L-ICPMS. *Microsc. Microanal.* **21**, 1229–1230 (2015).
45. Yang, L. Raw data for “Release and re-enrichment of invisible gold in arsenian pyrite promoted by coupled dissolution-precipitation reactions”, <https://doi.org/10.6084/m9.figshare.25471537.v1> (2024).
46. Wood, S. A. Calculation of activity-activity and log fO<sub>2</sub>-pH diagrams. *Rev. Econ. Geol.* **10**, 81–96 (1998).
47. Cooke, D. R., Bull, S. W., Large, R. R. & McGoldrick, P. J. The importance of oxidized brines for the formation of Australian Proterozoic stratiform sediment-hosted Pb-Zn (Sedex) deposits. *Econ. Geol.* **95**, 1–18 (2000).

## Acknowledgements

We appreciate Editors Joe Aslin and Holly Stein for handling, and Drs. Evan Hastie and Sabina Strmic Palinkas for providing constructive comments and suggestions on the manuscript. We thank mine geologists in the Chang'an gold deposit for their kind help during our fieldwork and sampling permissions, Prof. Chang Xu and Dr. Dapeng Wen at the China University of Geosciences (Wuhan) for their comprehensive help with the EBSD analyses of pyrite. This work was supported by the National Natural Science Foundation of China (42125203, 42102107, 42372110), the “Deep-time Digital Earth” Science and Technology Leading Talents Team Funds from the Central Universities for the Frontiers Science Center for Deep-time Digital Earth, China University of Geosciences (Beijing) (2652023001), and the 111 Project of the Ministry of Science and Technology (BP0719021). The IONTOF M6 ToF-SIMS at the John de Laeter Centre, Curtin University was funded by the Australian Research Council LIEF program (LE190100053).

## Author contributions

Conceptualization: L.Y., Q.F.W. and J.D. SEM, EBSD, and EPMA work: L.Y. and H.J.L. FIB and TEM work: L.Y. and H.Y.X. ToF-SIMS work: R.X.W. and W.R. Thermodynamic modeling: H.J.L. Data analysis: L.Y., Q.F.W., H.Y.X., and D.F. Writing—original draft: L.Y., Q.F.W., J.D. and D.G. Writing—review & editing: all authors.

## Competing interests

The authors declare no competing interests.

## Additional information

**Supplementary information** The online version contains supplementary material available at <https://doi.org/10.1038/s43247-024-01408-5>.

**Correspondence** and requests for materials should be addressed to Qingfei Wang or Jun Deng.

**Peer review information** *Communications Earth and Environment* thanks Evan Hastie, Sabina Strmic Palinkaš, and [name] for their contribution to the peer review of this work. Primary Handling Editors: Holly Stein and Joe Aslin. A peer review file is available.

**Reprints and permissions information** is available at <http://www.nature.com/reprints>

**Publisher's note** Springer Nature remains neutral with regard to jurisdictional claims in published maps and institutional affiliations.

**Open Access** This article is licensed under a Creative Commons Attribution 4.0 International License, which permits use, sharing, adaptation, distribution and reproduction in any medium or format, as long as you give appropriate credit to the original author(s) and the source, provide a link to the Creative Commons licence, and indicate if changes were made. The images or other third party material in this article are included in the article's Creative Commons licence, unless indicated otherwise in a credit line to the material. If material is not included in the article's Creative Commons licence and your intended use is not permitted by statutory regulation or exceeds the permitted use, you will need to obtain permission directly from the copyright holder. To view a copy of this licence, visit <http://creativecommons.org/licenses/by/4.0/>.

© The Author(s) 2024